

Modeling of a vertical tunneling graphene heterojunction field-effect transistor

S. Bala Kumar, Gyungseon Seol and Jing Guo^{a)}

Department of Electrical and Computer Engineering, University of Florida, Gainesville, FL,
32611

^aCorresponding author. E-mail: a) guoj@ufl.edu

Abstract

Vertical tunneling field-effect-transistor (FET) based on graphene heterojunctions with layers of *h*BN is simulated by self-consistent quantum transport simulations. It is found that the asymmetric p-type and n-type conduction is due to work function deference between the graphene contact and the tunneling channel material. Modulation of the bottom-graphene-contact plays an important role in determining the switching characteristic of the device. Due to the electrostatic short-channel-effects stemming from the vertical-FET structure, the output I-V characteristics do not saturate. The scaling behaviors the vertical-FET as a function of the gate insulator thickness and the thickness of the tunneling channel material are examined.

Graphene is an interesting material with unusual properties¹. This makes graphene a promising material for future electronic devices.² One of the proposed applications of graphene is the graphene-based field-effect-transistor (FET). However, the absence of bandgap in graphene would result in a high leakage current, and thus it would be difficult to turn off the transistor³. This effect is further worsen by Klein tunneling⁴ which allow electron tunneling across a potential barrier. As a result the ON-OFF ratio in a graphene based transistor is highly limited. Many methods have been proposed to overcome this problem, i.e. patterning of graphene nanoribbon⁵, applying electric field across multilayer graphene⁶, using quantum dots⁷ or chemical derivatives⁸. Recently an alternative vertical-tunneling-graphene (VTG) FET design was demonstrated⁹. This device, in which graphenes are used as contacts and not the channel, functions based on quantum tunneling across a thin insulating channel barrier such as layers of *h*BN or MoS₂, sandwiched between a pair of graphene contacts.

In this paper, we theoretically model the VTG-FET, investigate the qualitative behavior of the experimental observations and suggest methods for device optimization. We use a self-consistent capacitance model to obtain the electrochemical potential profile across the device, and then using non-equilibrium-greens-function (NEGF)¹⁰ method, we compute the current and conductance across the device. Unlike conventional transistors, where the source-drain contact simply play a passive role as reservoir of electrons, the operation of this device is primarily determined by the modulation of density-of-state (DOS) in the contacts, which is tuned by the applied gate and source-drain voltage. Due to the short-channel-effect, arising from the vertical structure, the I-V output of this device does not saturate. We also investigate the effect of channel and insulator thickness on optimizing performance of this device.

Our modeled device consists of a tunneling channel made of layered-*h*BN sandwiched between two graphene layers as shown in Fig. 1(a), similar to the structure demonstrated by L. Britnell et al.⁹ The graphene layers act as the source and drain contacts. The source-drain bias, V_b and the bottom gate voltage, V_g are applied as in Fig. 1(a). First we use a capacitance model to calculate the electrochemical potential at graphene and the *h*BN layers. Here, we explain the computation for a device with the channel consisting of a monolayer *h*BN. The charge at each layer-*i*, Q_i is related to the vacuum energy level, E_i as follows:

$$-Q_i = C_i (E_{i-1}^{vac} - E_i^{vac}) + C_{i+1} (E_{i+1}^{vac} - E_i^{vac}), \quad i = 0, 1, 2, 3, 4 \quad (1)$$

,where the capacitance $C = \epsilon_0 \epsilon_r / d$, ϵ_r is the dielectric constant and d is the thickness. Referring to Fig 1(b) and setting the boundaries $C_0=C_4=0$ and $E_{-1}^{vac} = E_4^{vac} = 0$, Eq. 1 can be expressed as

$$\begin{bmatrix} C_1 & -C_1 & & \\ -C_1 & C_1 + C_2 & -C_2 & \\ & -C_2 & C_2 + C_3 & -C_3 \\ & & -C_3 & C_3 \end{bmatrix} \begin{bmatrix} E_0^{vac} \\ E_1^{vac} \\ E_2^{vac} \\ E_3^{vac} \end{bmatrix} = \begin{bmatrix} -eQ_0 \\ -eQ_1 \\ -eQ_2 \\ -eQ_3 \end{bmatrix}, \text{ and further simplified to}$$

$$\begin{bmatrix} E_1^{vac} \\ E_2^{vac} \\ E_3^{vac} \end{bmatrix} = \begin{bmatrix} C_1 + C_2 & -C_2 & \\ -C_2 & C_2 + C_3 & -C_3 \\ & -C_3 & C_3 \end{bmatrix}^{-1} \begin{bmatrix} -eQ_1 + C_1 E_0^{vac} \\ -eQ_2 \\ -eQ_3 \end{bmatrix} \quad (2)$$

Note that $E_0^{vac} = -eV_g + \phi_g$, where ϕ_g is the bottom gate work function. From the value of E_i^{vac} obtained in Eq. 2, the charge density, Q_i is computed

$$Q_i = -e \int_{U_i}^{\infty} D_i(E) f_i^e(E) dE + e \int_{-\infty}^{U_i} D_i(E) f_i^p(E) dE \quad (3)$$

$U_i = E_i^{vac} - \phi_i$ is the source Dirac-point energy (E_s^{dir}), channel mid-gap energy (E^{mid}), and drain Dirac-point energy (E_D^{dir}) when $i=1,2$, and 3 respectively. D is the density-of-state (DOS) and $f^{e(p)}$ is the electron (hole) occupancy. Eq. 2 and 3 is then solved self-consistently until U_i converges. For *hBN* with more number of layers, the above equations are modified accordingly. The U_i profile across the device at flat band condition (when an arbitrary V_g and V_b is applied) is illustrated in Fig. 1(c) (Fig. 1(d)). Unless otherwise stated we use the following parameters for the simulation: SiO_2 insulator thickness, $t_{ins}=300\text{nm}$ and SiO_2 dielectric $\epsilon_{ins}=4$. The work function of the Si gate, graphene source/drain contacts and *hBN* channel are $\phi_g=4\text{eV}$, $\phi_{SD}=4.7\text{eV}^{11}$ and $\phi_c=3\text{eV}$, respectively. The distance between graphene contacts and the *hBN* channel is 0.5nm . *hBN* interlayer distance is 0.35nm^{12} . Number of channel layers, $N=3$. Note that $U_0=-eV_g$, $U_1=E_s^{dir}$, and $U_{N+3}=E_D^{dir}$. U_2 to U_{N+2} is equal to the E^{mid} of each *hBN* layers.

The electron transport behavior across the device is studied by using NEGF formalism¹⁰. The Hamiltonian of the monolayer *hBN* using π -orbital tight bonding model is given by

$$H(K) = \begin{bmatrix} E^{mid} + E_{gap}/2 & -t_0 - 2t_0 e^{+iK_x} \cos K_y \\ -t_0 - 2t_0 e^{-iK_x} \cos K_y & E^{mid} - E_{gap}/2 \end{bmatrix} \quad (4)$$

where $K_y = \sqrt{3}k_y a_0/2$, $K_x = 3k_x a_0/2$, intralayer nearest-neighbor (NN) hoping parameter, $t_0=2.3\text{eV}^{12}$, bandgap of the monolayer *hBN*, $E_{gap}=5\text{eV}^{13}$, and the NN intralayer atomic distance $a_0=0.15\text{nm}$. For multilayer *hBN*, we use AB-stacking *hBN* layers with interlayer hoping parameter, $t_p=0.6\text{eV}^{12}$. In the NEGF formalism, the electron transport across the device for a given energy E is

$$T(E) = \sum_K \text{Tr}[\Gamma_S(E)G(E, K)\Gamma_D(E)G(E, K)^\dagger] \quad (5)$$

where $G(E, K) = [EI - H(K) - \Sigma_S(E) - \Sigma_D(E)]^{-1}$ is the retarded Green's function of the GNR channel, $\Sigma(E)$ is the self energy coupling to the graphene contacts, and $\Gamma(E) = i[\Sigma(E) - \Sigma^+(E)]$. The subscript S(D) refers to the source (drain) contacts. For the self energy, the top and bottom, hBN layers are connected to the respective graphene contacts with a contact broadening of $\sigma = \beta |E - E^{\text{dir}}| L(E^{\text{dir}}, \gamma)$, where $L(E^{\text{dir}}, \gamma) = \frac{\gamma/\pi}{(E - E^{\text{dir}})^2 + \gamma^2}$ is the Lorentzian broadening function. Unless otherwise stated, we use $\beta = 0.01$ and $\gamma = 0.01\text{eV}$. Note that this expression is obtained by using the linear DOS of graphene, where the DOS is zero at the Dirac point, E^{dir} . Therefore the transmission is minimum when $E = E^{\text{dir}}$. We define $T_S(E) = T(E)/S$, S is the total area of the Brillouin zone used in Eq. 5. At a finite temperature, τ the areal-conductance across the graphene, at Fermi energy, E_F is

$$G_D(E_F) = g_0 \int_{-\infty}^{+\infty} T_S(E_F) \frac{1}{4k_B\tau} \text{sech}^2 \left(\frac{E - E_F}{2k_B\tau} \right) dE \quad (6)$$

, where $g_0 = e^2/h$ and k_B is the Boltzmann constant. When a finite bias is applied, the areal-source-drain current,

$$I_{SD} = g_0 \int_0^{qV_b} T_S(E) (f_S(E) - f_D(E)) dE \quad (7)$$

, where Fermi distribution function, $f_{S/D}(E) = \left(1 + \exp \left(\frac{E - \mu_{S/D}}{k_B\tau} \right) \right)^{-1}$, $\mu_S = 0$, and $\mu_D = eV_b$. The applied V_b and V_g changes the $H(K)$ in Eq. 4, and thus varies G_D and I_{SD} .

Fig. 2(a) shows the G_D - V_g curve obtained from our calculation. These results show a very good qualitative agreement with the experimental results from ref. 9, which is replotted in Fig. 2(b). We first investigate the ambipolar behavior observed in the G_D - V_g curve. One interesting feature of this device is that the qualitative behavior of the transport is strongly determined by the graphene bottom-contact, unlike in conventional transistors where the contacts play only a passive role. Therefore, in this VTG-FET, contact modulation is more critical, compared to channel barrier modulation. The non-uniform DOS in graphene, in contrast to the constant DOS in metallic contacts, results in the contact modulation. In graphene, DOS is zero at the Dirac point, and hence minimum transmission is obtained at the E^{dir} , even though in intrinsic *h*BN layers, the minimum transmission is obtained at the E^{mid} . Thus, as shown in Fig. 2(c-e), the alignment of graphene Dirac points relative to the E_F strongly affects the electron transport across the heterojunction between the bottom graphene contact and the channel.

Since Fig. 2(d) shows the zero bias conductivity, G_D . i.e. $V_b=0$, the Fermi energy is located at $E_F=\mu_S=\mu_D=0$. Referring to Fig. 2 (c-e), the minimum conductance, which is proportional to the minimum leakage current, is obtained when the Fermi level, E_F is aligned with the graphene Dirac point, i.e. $E_S^{dir} = E_D^{dir} = 0$. This condition is achieved when $V_g=V_{FB}\approx-1eV$, where V_{FB} is the flat band (FB) voltage. When $|V_g-V_{FB}|>0$, the DOS in graphene contacts become larger, and thus the G_D increases. Therefore we see an ambipolar behavior. We further study the effect of the quality of the contacts. Quantitatively, the quality of the contacts is model by increasing the broadening of the DOS in the contacts, γ . As shown in the inset of Fig. 2 (c), when the γ increases the ambipolar behavior gradually disappears, while the minimum leakage current increases. For example, at $\gamma=0.1eV$ the G_D decreases monotonically with increasing V_g ,

and the minimum leakage current is 10 times larger than when $\gamma = 0.01\text{eV}$. The contact modulation, as well as the minimum leakage current is also enhanced by the quality of the contact. In the experimental results in ref. 9, *h*BN is used as the insulator in between SiO_2 and graphene. It has been shown that graphene grown on a *h*BN substrate are of high quality¹⁴. Furthermore, graphene also forms a good contact with *h*BN channel due to similarity in atomic structure. Therefore, due to this high quality contact, the modulation of the contact DOS strongly affects the conductance across the *h*BN.

Another interesting feature in the Fig. 2(a), is the asymmetry of the G_D - V_g curve. The magnitude of the gradient of the G_D - V_g curve is not the same for $V_g < V_{FB}$ and $V_g > V_{FB}$. This asymmetric behavior is mainly caused by the different work function of the graphene contact and the channel material. As shown in Fig. 3(a-c), at FB, if $\phi_{SD} > \phi_C$ ($\phi_{SD} < \phi_C$), the Fermi level is closer to the valence (conductance) band, and hence the channel layer is a p(n)-type semiconductor. As a result, higher conductance is obtained when $V_g < V_{FB}$ ($V_g > V_{FB}$). In our structure, $\phi_{SD} > \phi_C$, and thus the Fermi level is closer to the valence band. Therefore at FB, the channel is a p-type semiconductor, in which the transmission is mainly due to the holes and thus gradient is higher when $V_g < V_{FB}$. We further quantify the asymmetry of the curve as $\alpha = -g_m^- / g_m^+ - 1$, where g_m^- (g_m^+) is the gradient of G_D - V_g curve when $V_g < V_{FB}$ ($V_g > V_{FB}$). Note that $\alpha > 0$ ($\alpha < 0$) indicates the curve is asymmetric with larger gradient when $V_g < V_{FB}$ ($V_g > V_{FB}$) and $\alpha = 0$ indicates that the curve is perfectly symmetric. Referring to Fig. 3(d-e), when we hypothetically vary the work function of the channel, the asymmetry is varied. When $\phi_{SD} = \phi_C$, where the channel is an intrinsic semiconductor at the FB, the curve is symmetric, i.e. $\alpha = 0$. On the hand, when $\phi_{SD} < \phi_C$ ($\phi_{SD} > \phi_C$), the channel becomes a n-type

semiconductor at FB, and thus $\alpha < 0$ ($\alpha > 0$) indicating the conductance is higher for when $V_g > V_{FB}$ ($V_g < V_{FB}$). Note that in all these cases we only considered the case where at the FB the Fermi level is within the channel band gap. We also would like to highlight that a similar effect of work function difference on G_D - V_g asymmetric has also been observed in horizontal nanoribbon FET, when the different contact materials are used¹⁵.

Fig. 4(a) shows the I_{SD} - V_b curve calculated from our model, while Fig. 4(b) shows the I_{SD} - V_b curve from the experimental results⁹. A good qualitative agreement is observed. One striking feature of these results is that, unlike conventional FETs, the I_{SD} does not saturate. In horizontal, electrostatically well designed FETs, the gate bias has much stronger control over the channel compared to the drain bias, which leads to a saturation of source-drain current. However, short channel length and stronger drain control degrades the saturation output characteristics. This phenomenon is known as drain-induced-barrier-lowering (DIBL) which occurs due to short-channel-effect in conventional FETs. A similar phenomenon is observed in this VTG-FET. Here, due to the ultra-thin channel length, i.e. in the order of 1nm, and due to the structure of the device, the gate voltage has less control over the channel potential. Therefore the drain bias causes significant change in the channel barrier, and thus the I_{SD} does not saturate. An effect reminiscent of DIBL is shown in Fig. 4(c-e), where the channel barrier is lowered by the increasing V_b , resulting in increasing current. It is also worth noting that the electronic transport in this VTG-FET is primarily due to the tunneling current. Referring to Fig. 4(c-e), as we increase the V_b the transmission window remains within the tunneling regime. The increasing of current with increasing V_b is caused by the decrease in the tunneling height.

Finally, we investigate the effect of channel thickness and bottom-gate insulator thickness, t_{ins} . The effect of channel thickness, which is proportional to the number of *h*BN layers N , is shown in Fig. 5(a). The increase of N is equivalent to an increase in barrier width and thus the electron tunneling decreases, exponentially decreasing the G_D . On the other hand, the increase in t_{ins} , does not change the minimal leakage current [Fig. 5(b)]. This is because, at FB, where the minimal leakage current is obtained, the contact potential is align with the Fermi level, $E_F=0$. The variation in t_{ins} does not effect this alignment, and thus the potential barrier within the device is independent of the t_{ins} . However, when the $V_g \neq V_{FB}$, the t_{ins} determines the potential profile across the device. The gate controllability of this potential profile increases with decreasing t_{ins} , resulting in a higher G_D , and thus increasing the ON-OFF ratio.

In conclusion, we study the electronic transport in a VTG-FET. This FET exhibits an ambipolar behavior similar to the recent experimental results. We also found an asymmetric p-type and n-type conduction is due to work function deference between the graphene contact and the tunneling channel material. The thin channel layer in VTG-FET, leads to a short channel effect, and thus the I_{SD} do not saturate when V_b is increased. Finally we showed that the increase in t_{ins} decreases the minimum leakage current, while the variation in insulator thickness does not affect the minimum leakage current. The modeling work not only explains the major features observed in a recent experiment, but also indicates the importance of improving the quality of the bottom graphene contact and scaling down the gate insulator of the VTG-FET.

We would like to thank Prof. P. Kim of Columbia University for technical discussions. This work was supported by NSF and ONR.

Figure and Caption

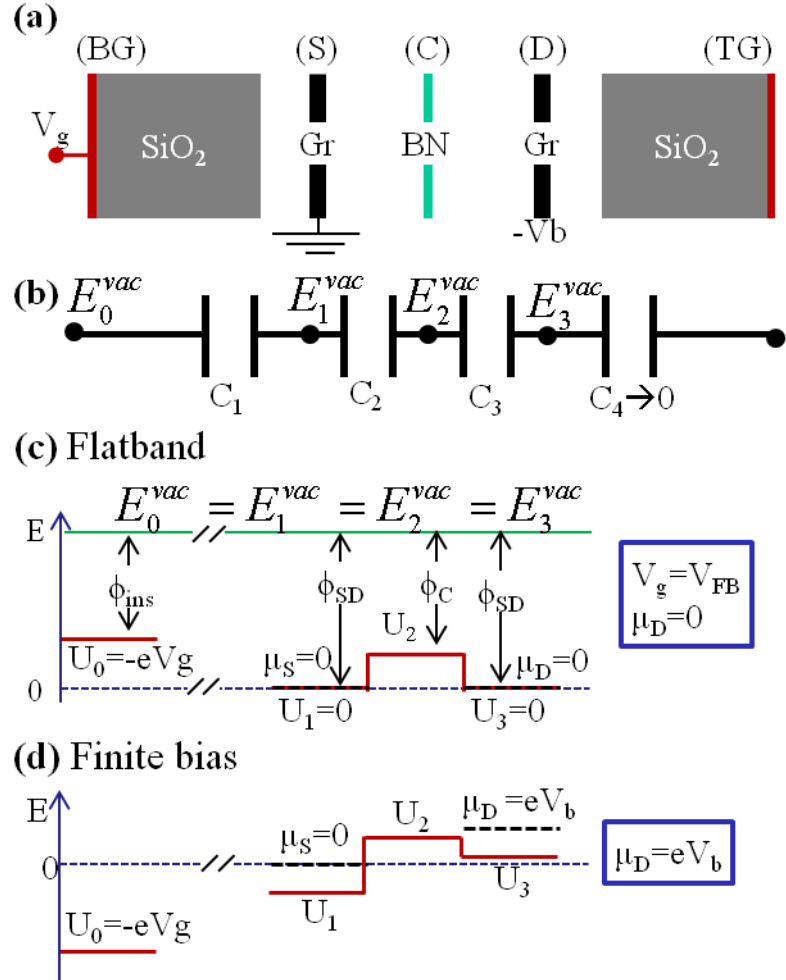


Figure 1 (a) Shows the device structure with a monolayer hBN as the channel. TG, S, C, D, and BG represent top-gate source, channel, drain, and bottom-gate respectively. Gr refers to graphene. (b) The capacitance model corresponding to (a). E^{vac} is the vacuum energy level. The potential profile across the device (c) at flatband condition, and (d) when an arbitrary V_g and V_b is applied. ϕ_g , ϕ_{SD} , ϕ_C refers to the gate, source/drain, and channel workfunctions, respectively. The BG potential, $U_0 = -eV_g$, Fermi energy at source (drain), $\mu_S = 0$ ($\mu_D = eV_b$). The potential definitions are consistent with ref. 9. $U_{1(3)}$ is the graphene Dirac point energy at source (drain), while U_2 is the midgap energy of the channel.

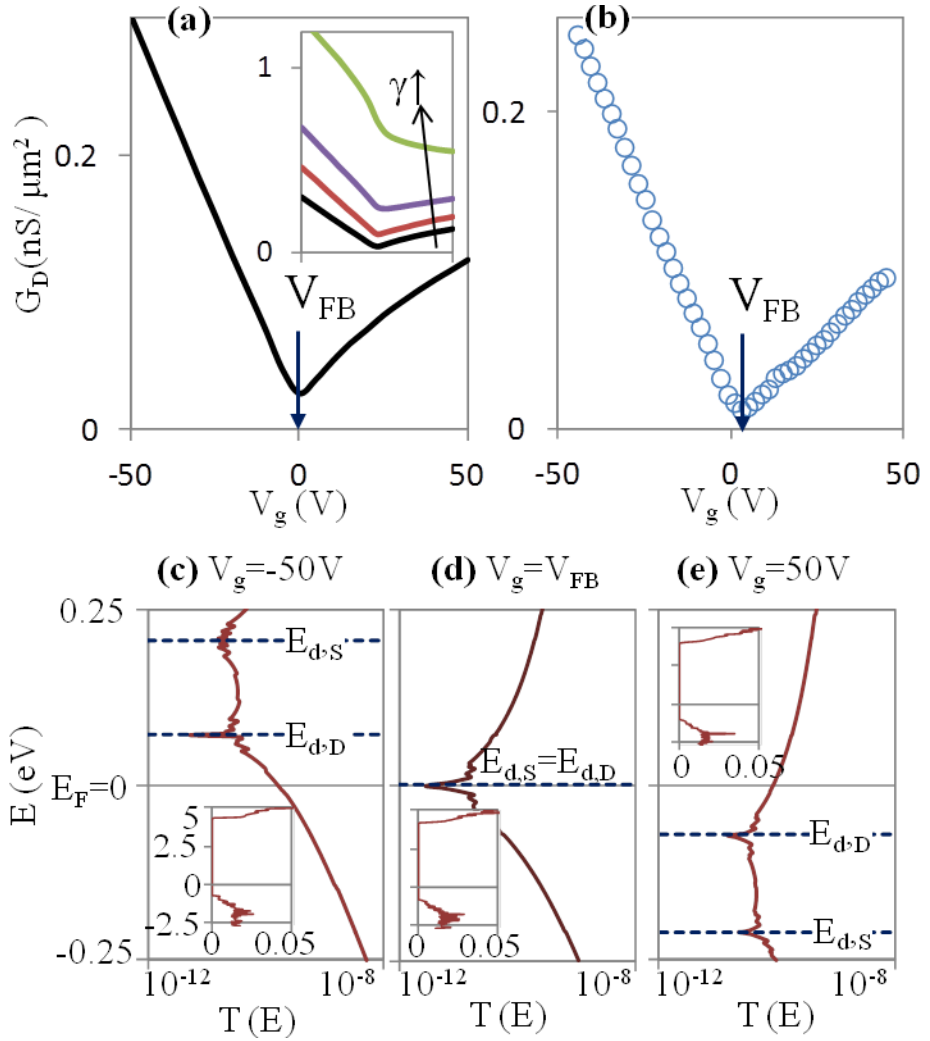


Figure 2 (a) G_d - V_g curve at $V_b=0$. The inset shows G_d with varying contact broadening, γ [$\gamma=0.01, 0.05, 0.1, 0.5\text{eV}$]. (b) Experimental results obtain in ref. 9, showing a good qualitative agreement with (a). The transmission curve in log scale for (c) $V_g < V_{FB}$, (d) $V_g = V_{FB}$, and (e) $V_g > V_{FB}$ at the vicinity of Fermi level, $E_F=0$. The inset in (c-e) show the transmission in linear scale for a larger energy range.

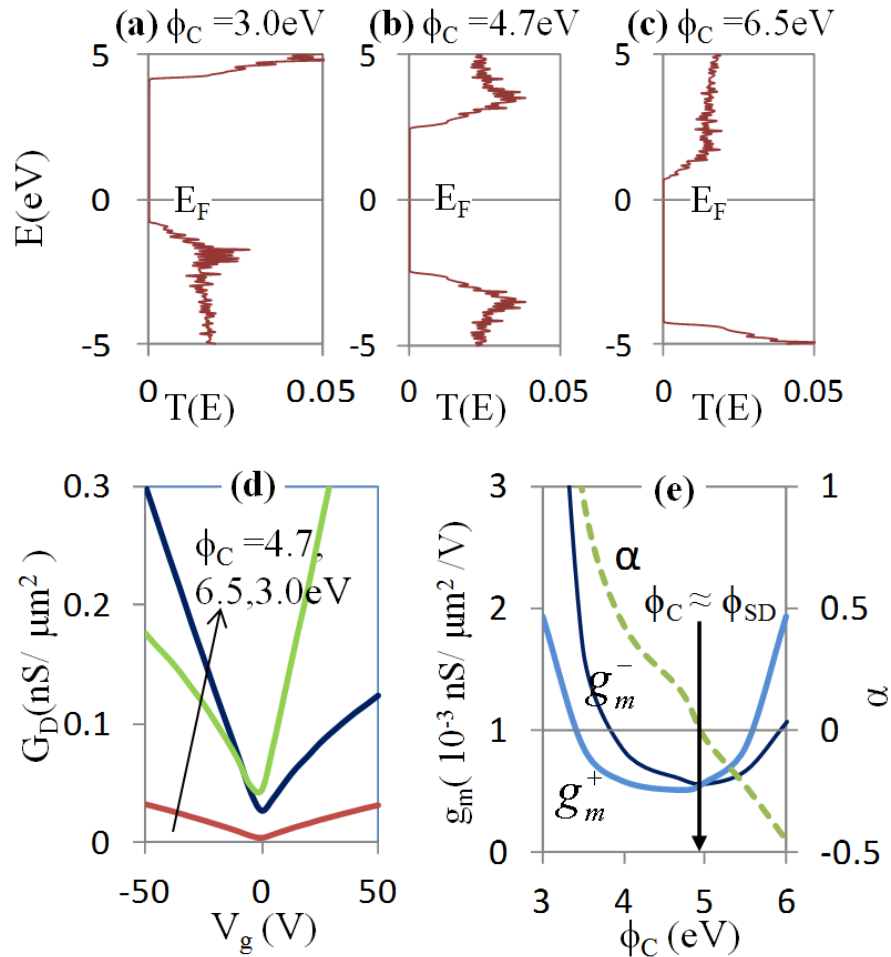


Figure 3 Transmission curve at FB for (a) $\phi_C < \phi_{SD}$, (b) $\phi_C = \phi_{SD}$, (c) $\phi_C > \phi_{SD}$. The channel varies from a p-type to n-type semiconductor as the ϕ_C increases. (d) Shows G_D - V_g for different ϕ_C values. (e) g_m^+ , g_m^- , and α variation as a function of ϕ_C . When $\phi_C \approx \phi_{SD}$, $g_m^- = g_m^+$ resulting in $\alpha = 0$, i.e. a symmetric G_D - V_g curve.

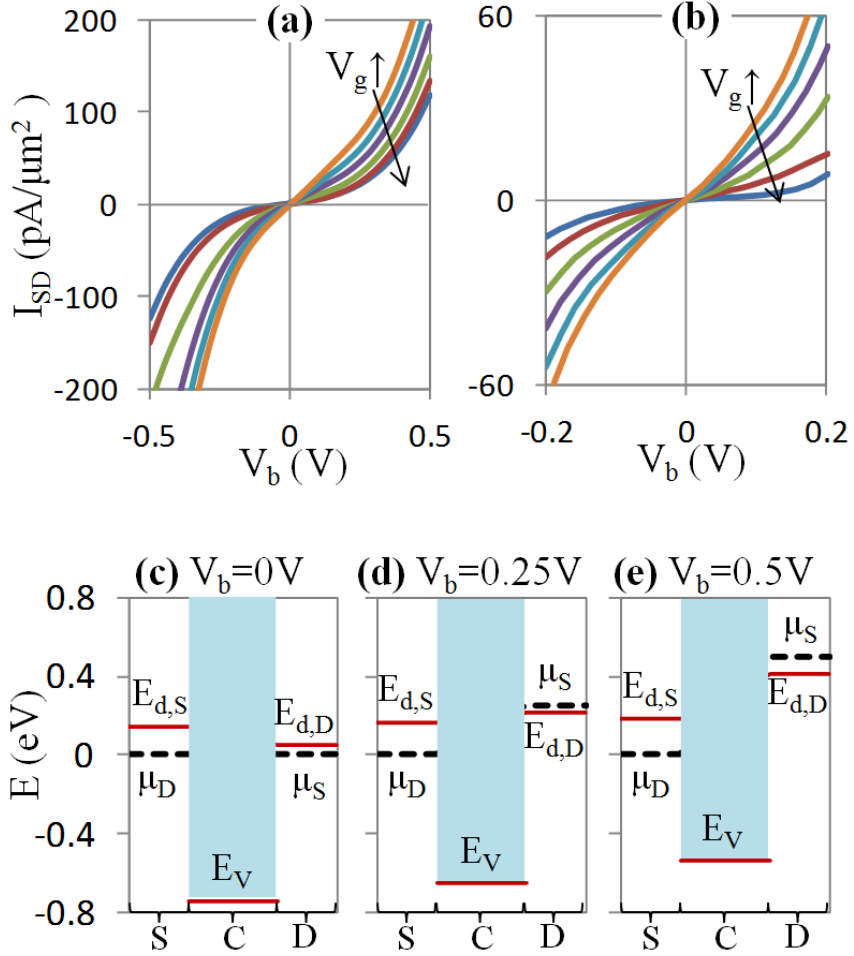


Figure 4 (a) I_{SD} - V_b curve for different V_g values. V_g is varied from -45V to 5V in a step of 10V. (b) Experimental results obtain in ref. 9, showing a good qualitative agreement with (a). The potential profile across the device when (c) $V_b=0\text{V}$, (d) $V_b=0.25\text{V}$, and (e) $V_b=0.5\text{V}$. The shaded region indicates band gap. The channel potential is decreases with increasing V_b , reminiscent of drain-induced-barrier-lowering effect (DIBL).

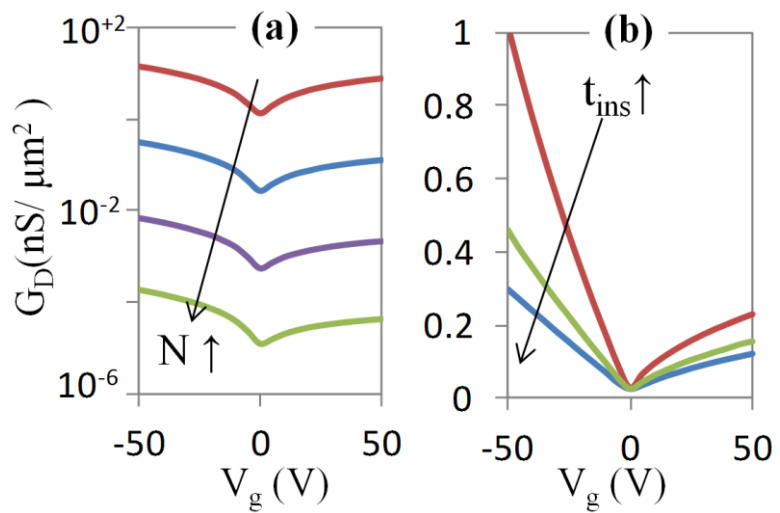


Figure 5 (a) Shows G_D - V_g for different N values. [$N=2, 3, 4, 5$]. (b) Shows G_D - V_g for different t_{ins} values. [$t_{\text{ins}}=100, 200, 300$ nm].

References

¹ A. K. Geim and K. S. Novoselov, *Nature Materials* **6** (3), 183 (2007); A. H. Castro Neto, F. Guinea, N. M. R. Peres, K. S. Novoselov, and A. K. Geim, *Reviews of Modern Physics* **81** (1), 109 (2009).

² Yuanbo Zhang, Yan-Wen Tan, Horst L. Stormer, and Philip Kim, *Nature* **438** (7065), 201 (2005); K. S. Novoselov, A. K. Geim, S. V. Morozov, D. Jiang, Y. Zhang, S. V. Dubonos, I. V. Grigorieva, and A. A. Firsov, *Science* **306** (5696), 666 (2004).

³ Phaedon Avouris, Zhihong Chen, and Vasili Perebeinos, *Nat Nano* **2** (10), 605 (2007); A. K. Geim, *Science* **324** (5934), 1530 (2009); Frank Schwierz, *Nat Nano* **5** (7), 487 (2010).

⁴ M. I. Katsnelson, K. S. Novoselov, and A. K. Geim, *Nat Phys* **2** (9), 620 (2006); Vadim V. Cheianov and Vladimir I. Fal'ko, *Physical Review B* **74** (4), 041403 (2006); N. Stander, B. Huard, and D. Goldhaber-Gordon, *Physical Review Letters* **102** (2), 026807 (2009); Andrea F. Young and Philip Kim, *Nat Phys* **5** (3), 222 (2009).

⁵ Melinda Y. Han, Barbaros Özyilmaz, Yuanbo Zhang, and Philip Kim, *Physical Review Letters* **98** (20), 206805 (2007); Xiaolin Li, Xinran Wang, Li Zhang, Sangwon Lee, and Hongjie Dai, *Science* **319** (5867), 1229 (2008).

⁶ Eduardo V. Castro, K. S. Novoselov, S. V. Morozov, N. M. R. Peres, J. M. B. Lopes dos Santos, Johan Nilsson, F. Guinea, A. K. Geim, and A. H. Castro Neto, *Physical Review Letters* **99** (21), 216802 (2007); Jeroen B. Oostinga, Hubert B. Heersche, Xinglan Liu, Alberto F. Morpurgo, and Lieven M. K. Vandersypen, *Nat Mater* **7** (2), 151 (2008).

⁷ Christoph Stampfer, Stefan Fringes, Johannes Güttinger, Francoise Molitor, Christian Volk, Bernat Terrés, Jan Dauber, Stephan Engels, Stefan Schnez, Arnhild Jacobsen, Susanne Dröscher, Thomas Ihn, and Klaus Ensslin, *Frontiers of Physics* **6** (3), 271 (2011).

⁸ D. C. Elias, R. R. Nair, T. M. G. Mohiuddin, S. V. Morozov, P. Blake, M. P. Halsall, A. C. Ferrari, D. W. Boukhvalov, M. I. Katsnelson, A. K. Geim, and K. S. Novoselov, *Science* **323** (5914), 610 (2009).

⁹ L. Britnell, R. V. Gorbachev, R. Jalil, B. D. Belle, F. Schedin, A. Mishchenko, T. Georgiou, M. I. Katsnelson, L. Eaves, S. V. Morozov, N. M. R. Peres, J. Leist, A. K. Geim, K. S. Novoselov, and L. A. Ponomarenko, *Science* **335** (6071), 947 (2012).

¹⁰ S. Datta, *Quantum Transport: Atom to Transistor*. Cambridge University Press, Cambridge, (2005).

¹¹ Young-Jun Yu, Yue Zhao, Sunmin Ryu, Louis E. Brus, Kwang S. Kim, and Philip Kim, *Nano Letters* **9** (10), 3430 (2009).

¹² R. M. Ribeiro and N. M. R. Peres, *Physical Review B* **83** (23), 235312 (2011).

¹³ Dmitri Golberg, Yoshio Bando, Yang Huang, Takeshi Terao, Masanori Mitome, Chengchun Tang, and Chunyi Zhi, *ACS Nano* **4** (6), 2979 (2010).

¹⁴ C. R. Dean, A. F. Young, MericL, LeeC, WangL, SorgenfreiS, WatanabeK, TaniguchiT, KimP, K. L. Shepard, and HoneJ, *Nat Nano* **5** (10), 722 (2010).

¹⁵ Ali Javey, Jing Guo, Qian Wang, Mark Lundstrom, and Hongjie Dai, *Nature* **424** (6949), 654 (2003); R. Martel, V. Derycke, C. Lavoie, J. Appenzeller, K. K. Chan, J. Tersoff, and Ph Avouris, *Physical Review Letters* **87** (25), 256805 (2001).